OPTICA

Ultrahigh-Q on-chip silicon–germanium microresonators

Ryan Schilling,* Chi Xiong, Swetha Kamlapurkar, Abram Falk, Nathan Marchack, Stephen Bedell, Richard Haight, Christopher Scerbo, Hanhee Paik, and Jason S. Orcutt

IBM Quantum, T.J. Watson Research Center, 1101 Kitchawan Road, Yorktown Heights, New York 10598, USA
**Corresponding author: ryan.schilling@alumni.epfl.ch*

Received 18 November 2021; revised 4 February 2022; accepted 5 February 2022; published 4 March 2022

To date, integrated waveguides with the lowest losses have all relied at least in part on amorphous materials. In this work, we demonstrate fully crystalline, single-mode integrated microresonators comprising epitaxially grown $Si_{0.86}Ge_{0.14}$ waveguide cores with silicon claddings. This platform supports ultrahigh-quality-factor resonances, with Q reaching $1.71 \pm 0.06 \times 10^8$, corresponding to a loss rate of 0.39 ± 0.02 dB/m. This Q is nearly an order-of-magnitude improvement over that seen in prior integrated Si waveguides. Together with silicon's strong Kerr nonlinearity, our results could unlock important new avenues for microwave photonics, optomechanics, and quantum transduction.

https://doi.org/10.1364/OPTICA.448469

Whispering gallery mode resonators, which use continuously curved loops to guide electromagnetic waves by total internal reflection, have been extensively studied for more than half a century due to their ability to support very high quality factors (Q). The highest Q resonators have been fabricated with macroscopic machining techniques, such as manually polishing Si [1] and melting silica fibers into spheres [2], resulting in $Q > 10^9$ in both cases. An extensive effort is now underway to microfabricate resonators that can match or even exceed these Q values. Indeed, in amorphous systems, recent progress has significantly narrowed the gap between the quality of macroscopic and microfabrication processes. The best results for integrated silica resonators use wet etching to achieve $Q = 2.1 \times 10^8$ [3]. Recent progress in silicon nitride devices has utilized high-temperature annealing to demonstrate $Q = 4.2 \times 10^8$ [4]. However, there remains a large gap in the performance of Si resonators. Despite much effort invested in silicon photonics, the best Q achieved in silicon resonators has been $Q = 2.2 \times 10^7$ and requires a silica top cladding [5]. Compared to silica and silicon nitride, silicon has a much higher Kerr nonlinearity and exceptionally low microwave loss, making it a desirable waveguide platform for nonlinear optical and quantum optical applications interfacing with superconducting microwave circuits.

The many benefits of integrated optical resonators, including their capability of forming more complicated optical circuits and their compatibility with proximate electrodes, has led to their use in many applications [6–11]. Typically, these applications, such as Kerr combs [12] and microwave-optical quantum transducers [13,14], also demand high intrinsic Q. For that reason, there is broad interest in improving the performance of on-chip silicon resonators. By significantly improving the Q of silicon-based integrated photonic resonators in this work, we are taking a major step toward bridging the disparity in optical loss between microfabricated amorphous dielectric and crystalline silicon systems.

Our fully monocrystalline and epitaxial waveguide platform comprises a low-mole-fraction silicon–germanium core that is fully clad by silicon. Optical losses due to pinned surfaces resulting in free-carrier and/or defect-state absorption are eliminated by extending the single-crystalline region throughout the region occupied by the optical mode. Furthermore, scattering losses are minimized by the low-index contrast of our Si_xGe_{1-x} waveguide relative to its Si cladding (an order of magnitude lower than that of Si relative to SiO_2).

Although Si_xGe_{1-x} waveguides have attracted attention for linear and nonlinear applications [15,16], the lowest propagation loss in a Si_xGe_{1-x} waveguide at telecom wavelengths was reported to be 65 dB/m in $Si_{0.9}Ge_{0.1}$ waveguides [17]. In contrast, our optimization of waveguide loss focuses on maintaining a fully strained Si_xGe_{1-x} layer, which is achieved through experimental determination of the maximum metastable thickness, as well as minimizing thermal shock and thermal budget during the epitaxial silicon cladding growth. In addition, we focus on minimizing processing contamination that can lead to interface defects. We are thus able to achieve a loss rate of 0.39 ± 0.02 dB/m. With a fully strained Si_xGe_{1-x} waveguide core and epitaxial silicon cladding, the core/cladding index contrast can be optimized, and defect-state absorption minimized.

Our waveguides are defined in epitaxial $Si_{0.86}Ge_{0.14}$ layers that are grown on high-resistivity Cz-Si wafers via chemical vapor deposition (see Supplement 1 S1). An important performance parameter is the $Si_{0.86}Ge_{0.14}$ thickness. If it is too thin, curvature-induced radiation will limit the waveguide loss. On the other hand, when $Si_{0.86}Ge_{0.14}$ is grown beyond the Matthews–Blakeslee

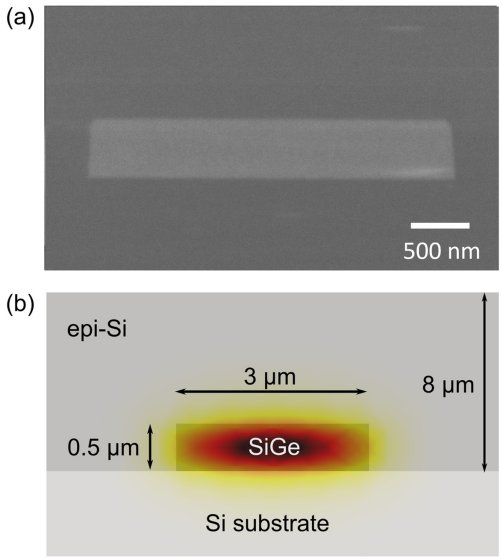

Fig. 1. (a) SEM of $Si_{0.86}Ge_{0.14}$ resonator core surrounded by epitaxial silicon. (b) Corresponding dimensions of the waveguide and cladding layer with overlaid finite element model of TE-like mode electric field at 1550 nm. The TE- (TM)-like modes have numerically calculated effective mode areas of 7.2 μm^2 (3.8 μm^2) and confinement factors of 0.34 (0.48).

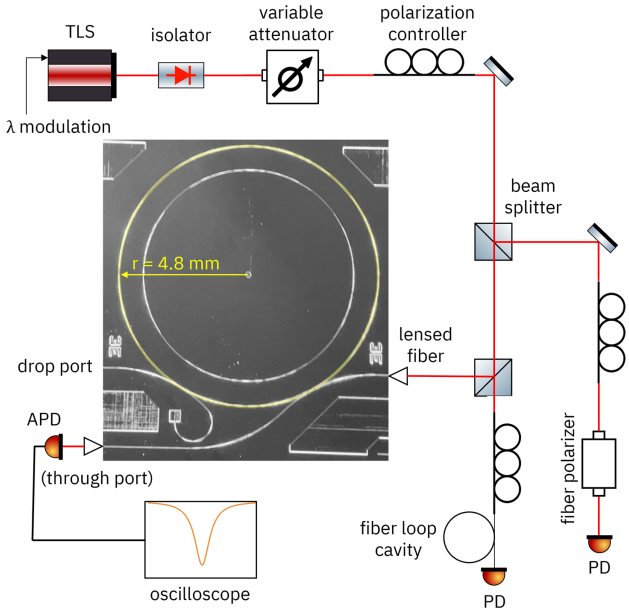

Fig. 2. Characterization setup used to measure transmission spectra around resonance at both through and drop ports. The input waveguide is seen at the right-side lensed fiber, and the through port is seen at the left-side lensed fiber (drop port is above). The ring resonator is highlighted in yellow.

critical thickness [18,19], plastic relaxation emerges that creates defects and degrades the strain. Thus, our target thickness for $Si_{0.86}Ge_{0.14}$ is near the expected metastable critical thickness observed in prior work [20]. The grown layers are determined to be fully strained within the precision of x-ray diffraction (XRD) analysis and then more precisely evaluated with defect-selective etching (see Supplement 1 S5). Waveguides are then defined in the $Si_{0.86}Ge_{0.14}$ by optical lithography followed by inductively coupled plasma (ICP) etching. The surface is then cleaned, and an epitaxial silicon cladding layer is grown on top, with a controlled ramp rate and minimum growth temperature to reduce relaxation of the $Si_{0.86}Ge_{0.14}$. A dichlorosilane (DCS) precursor is chosen for the epitaxial silicon top cladding to prevent keyholing in narrow waveguide gaps, which arises due to crystallographic orientation-dependent growth rates [21]. Careful control over the growth conditions is critical to maintain strain in the metastable films (see Supplement 1 S5). The chips are then either cleaved or diced from the wafer to expose the waveguide facets. Figure 1 shows the waveguide cross section and numerically calculated TE-like mode profile. All devices studied in this work employ a ring resonator with a radius of 4.8 mm, coupled to two (through/drop) waveguides with the same coupling gap.

Characterization is carried out using the setup shown in Fig. 2. A lensed fiber on a precision stage couples light into the input waveguide, and a second lensed fiber collects the light at either the through or drop port. Three wideband tunable diode lasers are used to collect the transmission port data (Figs. 3 and 4) over the range of 1300 nm to 1640 nm. For each measurement, the laser is tuned to the resonance wavelength of interest, and a function generator is used to modulate the laser cavity length to perform a narrow continuous sweep across the resonance. The optical power in the input waveguide is 10 μW, well beneath the threshold of nonlinear loss caused by two-photon absorption and the subsequent free-carrier absorption. Light is split off from the input fiber to a fiber loop cavity with a calibrated free-spectral range

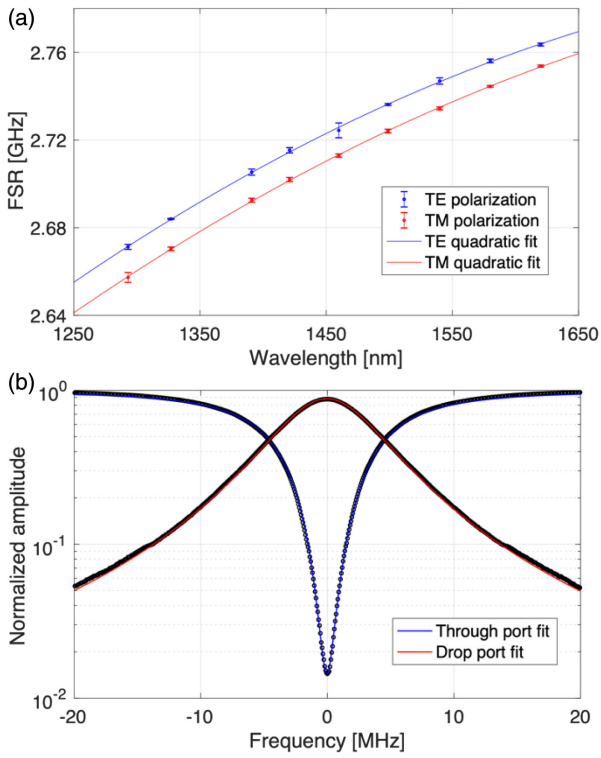

Fig. 3. (a) Extracted free-spectral ranges for both polarizations as a function of wavelength (one standard deviation error bars). Solid lines show a quadratic fit to the data. (b) Zoom-in and fitting to the through and drop port data to determine intrinsic loss rate of the TM mode at 1450 nm.

(FSR), which serves as a frequency reference for the narrow scan. Light is also split off to a pair of crossed polarizers that allows for tracking of the input polarization.

An example of this type of scan is shown in Fig. 3(b), where the input polarization has been tuned to the TM mode. Here, the through and drop port data have been fitted to extract the internal Q of the ring resonator itself. In this case, an internal $Q = 1.71 \pm 0.06 \times 10^8$ is measured for the TM mode at 1450 nm (see Supplement 1 S3 for Q extraction). This characterization was carried out for modes across a broad spectral range, for TM and TE polarizations (Fig. 4). For both, Q was maximized near 1450 nm, with a trend of decreasing Q at both shorter and longer wavelengths. The increasing loss at shorter wavelengths is attributed to the expected effect of band edge absorption. At longer wavelengths, the dominant loss mechanism for the TE mode is radiation loss deriving from to the bending of the waveguide. The TM mode, which has a higher effective index due to the birefringence of strained Si_xGe_{1-x}, is not radiation loss limited.

The radiation loss model plotted in Fig. 4(b) utilizes a single fitting parameter, which is the $Si_{0.86}Ge_{0.14}$ refractive index, n_{SiGe} (see Supplement 1 S4). The geometry of the modeled waveguide is fixed by the measured parameters of the physical waveguide. The fitted result for the in-plane (TE) index, implies $n_{SiGe,\,TE} = 1.013 n_{Si}$. The close agreement between data and radiation-loss-limited scaling in the L-band strongly suggests that radiation loss is the dominant loss mechanism.

The birefringence between TE and TM polarizations in our system is experimentally determined from quadratic fits to the polarization-dependent FSRs shown in Fig. 3(a), combined with numerical mode simulation (see Supplement 1 S4). Taking the difference of the quadratic fits allows us to establish the birefringence in terms of the ratio of group indices, $n_{g,\,TM}/n_{g,\,TE}$ (see Fig. S7). Using the in-plane index $(n_{SiGe,||}) = 1.013 n_{Si}$ determined from the radiation-loss model [Fig. 4(b) and Fig. S6] and a finite difference eigenmode (FDE) solver to translate between material and group indices, the out-of-plane refractive index $(n_{SiGe,\,\perp})$ is then determined to be $n_{SiGe,\,\perp} = 1.023 n_{Si}$ (see Fig. S8). Using the radiation-loss model for the TM mode, we determine that $n_{SiGe,\,\perp} \geq 1.015 n_{Si}$ is sufficient for the radiation-loss limit to exceed the Q measured in Fig. 4(a). These results agree fairly well with the result $n_{SiGe} = 1.0115 n_{Si}$ that was obtained through ellipsometry (see Supplement 1 S2), using an isotropic model for the refractive index.

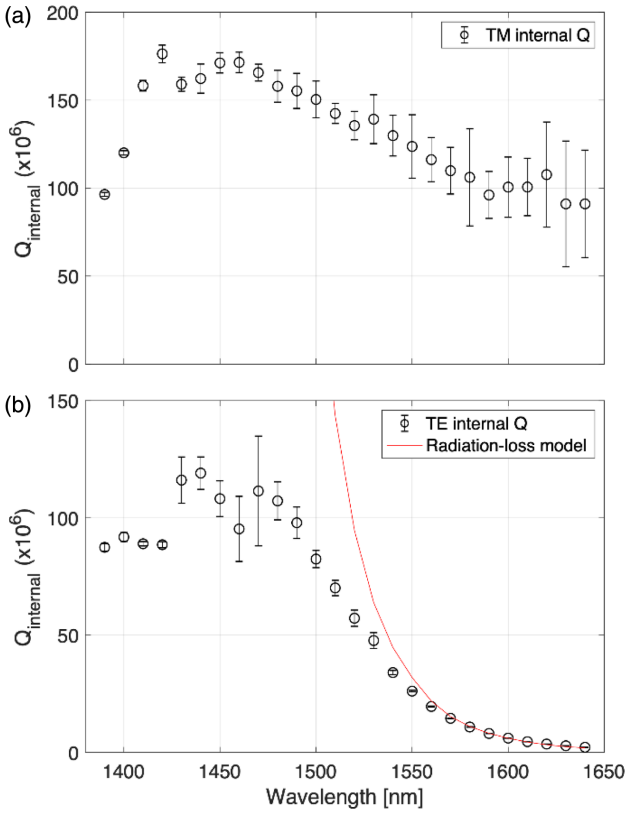

Fig. 4. Comparison of experimentally measured optical Q as a function of wavelength, for (a) TM and (b) TE polarizations in a single-mode microresonator (open circles, with one standard deviation error bars). Overlaid with a solid red line for TE is a radiation loss model utilizing the $Si_{0.86}Ge_{0.14}$ refractive index as a single fitting parameter.

A previous study of the polarization-dependent refractive index for pseudomorphic Si_xGe_{1-x} waveguides grown on Si also observed an anisotropy between the out-of-plane and in-plane indices [22]. This work, based on experimentally tracing out the mode profiles, determined an index difference of $n_{SiGe,\,\perp} - n_{SiGe,||} = (0.21 \pm 0.07)x$, for strained $Si_{1-x}Ge_x$ films. For $Si_{0.86}Ge_{0.14}$ studied in this work, the calculations above correspond to a birefringent index difference of $n_{SiGe,\,\perp} - n_{SiGe,||} = 0.24x$, in agreement with the prior literature.

As can be seen in Fig. 4(b) and Fig. S6, the agreement between experiment and radiation-limited Q does not hold at wavelengths below 1500 nm for the TE mode. In fact, at 1450 nm, the limit to Q imposed by curvature-derived radiation is nearly an order of magnitude higher than in the experiment. As discussed, the TM data are not radiation limited at any measured wavelength. Therefore, neither loss mechanism—band edge absorption nor radiation loss—is setting the Q limit in the E- and S-bands. Although the mechanism is not identified here, a likely candidate is scattering at the etched $Si_{0.86}Ge_{0.14}$/Si interface. At longer wavelengths, the Q may be degraded as a result of strong coupling to the bus waveguides leading to hybridization.

One of the main features of the radiation loss regime is the extreme sensitivity of Q to material and design parameters. For instance, in our regime, the calculated radiation-limited Q improves by three orders of magnitude by doubling R from 4.8 mm to 9.6 mm. Alternatively, increasing the Ge concentration from $Si_{0.86}Ge_{0.14}$ to $Si_{0.85}Ge_{0.15}$ would result in an order of magnitude lower radiative loss in the C-band (Fig. S6).

We have demonstrated an ultrahigh-Q on-chip silicon–germanium microresonator system with unprecedented low loss rates. It uses a novel fully crystalline design based on the low-refractive-index contrast between Si and $Si_{0.86}Ge_{0.14}$ to minimize interface scattering losses. Relative to the prior state-of-the-art for silicon ring resonators [5], our results improve waveguide loss by nearly an order of magnitude. Moreover, there is clear space to improve substantially on these current results by optimizing the Si_xGe_{1-x} growth process and exploring other Ge mole fractions. Currently, our Q values are nearly on par with the best on-chip, waveguide coupled microresonators, which are formed by wet etching of silica [3]. Moreover, our system has the added advantage of being single mode, allowing precise and reproducible control over dimensions by dry etching, being solid and thus immune to mechanical vibrations, and being hermitically sealed from the environment by way of an encapsulating silicon layer.

The Si_xGe_{1-x} system is also particularly well suited to build microwave-optical transducers for quantum state transfer [14]. In addition to the low optical losses demonstrated here, this epitaxial system has very low microwave losses, as has been recently demonstrated by the fabrication of transmon qubits with > 100 μs

coherence times on similar substrates [23]. Moreover, the low acoustic loss of silicon is expected to make this a favorable direction for optomechanics-based transducers [24,25]. Beyond transducers, the Si_xGe_{1-x} platform could enable significant improvements for a wide variety of devices, including compact spectrometers, precision mass sensors, and optically generated microwave sources.

Funding. Army Research Office (W911NF-18-1-0022).

Acknowledgment. The authors acknowledge support in device fabrication from the IBM Microelectronics Research Laboratory and IBM Central Scientific Services.

Disclosures. RS, CX, SK, AF, NM, SB, RH, CS, HP, JSO (E).

Data availability. Data underlying the results presented in this paper are not publicly available at this time but may be obtained from the authors upon reasonable request.

Supplemental document. See Supplement 1 for supporting content.

REFERENCES

1. A. E. Shitikov, I. A. Bilenko, N. M. Kondratiev, V. E. Lobanov, A. Markosyan, and M. L. Gorodetsky, Optica **5**, 1525 (2018).
2. L. Collot, V. Lefèvre-Seguin, M. Brune, J. M. Raimond, and S. Haroche, Europhys. Lett. **23**, 327 (1993).
3. K. Y. Yang, D. Y. Oh, S. H. Lee, Q.-F. Yang, X. Yi, B. Shen, H. Wang, and K. Vahala, Nat. Photonics **12**, 297 (2018).
4. M. W. Puckett, K. Liu, N. Chauhan, Q. Zhao, N. Jin, H. Cheng, J. Wu, R. O. Behunin, P. T. Rakich, K. D. Nelson, and D. J. Blumenthal, Nat. Commun. **12**, 934 (2021).
5. A. Biberman, M. J. Shaw, E. Timurdogan, J. B. Wright, and M. R. Watts, Opt. Lett. **37**, 4236 (2012).
6. K. J. Vahala, Nature **424**, 839 (2003).
7. W. Liang, V. S. Ilchenko, A. A. Savchenkov, E. Dale, D. Eliyahu, A. B. Matsko, and L. Maleki, Optica **4**, 114 (2017).
8. A. B. Matsko, D. V. Strekalov, and N. Yu, Phys. Rev. A **77**, 043812 (2008).
9. W. Liang, D. Eliyahu, V. S. Ilchenko, A. A. Savchenkov, A. B. Matsko, D. Seidel, and L. Maleki, Nat. Commun. **6**, 7957 (2015).
10. B. Min, T. J. Kippenberg, L. Yang, K. J. Vahala, J. Kalkman, and A. Polman, Phys. Rev. A **70**, 033803 (2004).
11. Q. Xu, B. Schmidt, S. Pradhan, and M. Lipson, Nature **435**, 325 (2005).
12. T. J. Kippenberg, R. Holzwarth, and S. A. Diddams, Science **332**, 555 (2011).
13. M. Tsang, Phys. Rev. A **81**, 063837 (2010).
14. J. Orcutt, H. Paik, L. Bishop, C. Xiong, R. Schilling, and A. Falk, Quantum Sci. Technol. **5**, 034006 (2020).
15. R. Claps, V. Raghunathan, O. Boyraz, P. Koonath, D. Dimitropoulos, and B. Jalali, Opt. Express **13**, 2459 (2005).
16. J. M. Ramirez, Q. Liu, V. Vakarin, J. Frigerio, A. Ballabio, X. L. Roux, D. Bouville, L. Vivien, G. Isella, and D. Marris-Morini, Opt. Express **26**, 870 (2018).
17. K. Hammani, M. A. Ettabib, A. Bogris, A. Kapsalis, D. Syvridis, M. Brun, P. Labeye, S. Nicoletti, D. J. Richardson, and P. Petropoulos, Opt. Express **21**, 16690 (2013).
18. J. W. Matthews and A. E. Blakeslee, J. Cryst. Growth **32**, 265 (1976).
19. R. People and J. C. Bean, Appl. Phys. Lett. **47**, 322 (1985).
20. J. M. Hartmann, A. Abbadie, and S. Favier, J. Appl. Phys. **110**, 083529 (2011).
21. L. Vescan, K. Grimm, and C. Dieker, J. Vac. Sci. Technol. B **16**, 1549 (1998).
22. M. Robillard, P. E. Jessop, D. M. Bruce, S. Janz, R. L. Williams, S. Mailhot, H. Lafontaine, S. J. Kovacic, and J. J. Ojha, J. Vac. Sci. Technol. B **16**, 1773 (1998).
23. M. Sandberg, V. Adiga, M. Brink, C. Kurter, C. Murray, M. Hopstaken, J. Bruley, J. S. Orcutt, and H. Paik, Appl. Phys. Lett. **118**, 124001 (2021).
24. M. Mirhosseini, A. Sipahigil, M. Kalaee, and O. Painter, Nature **588**, 599 (2020).
25. G. S. MacCabe, H. Ren, J. Luo, J. D. Cohen, H. Zhou, A. Sipahigil, M. Mirhosseini, and O. Painter, Science **370**, 840 (2020).